arXiv:1412.7904v1 [astro-ph.SR] 26 Dec 2014

PARTICLE ACCELERATION IN PLASMOID EJECTIONS DERIVED FROM RADIO DRIFTING PULSATING STRUCTURES

N. Nishizuka[1], M. Karlický[2], and M. Janvier[3], M. Bárta[2]

ABSTRACT

We report observations of slowly drifting pulsating structures (DPS) in the 0.8-4.5 GHz frequency range of the RT4 and RT5 radiospectrographs at Ondřejov Observatory, between 2002 and 2012. We found 106 events of drifting pulsating structures, which we classified into 4 cases: (I) single events with a constant frequency drift [12 events], (II) multiple events occurring in the same flare with constant frequency drifts [11 events], (III) single or multiple events with increasing or decreasing frequency drift rates [52 events], and (IV) complex events containing multiple events occurring at the same time in the different frequency range [31 events]. Many DPSs are associated with hard X-ray bursts (15-25 keV) and soft X-ray gradient peaks, as they typically occurred at the beginning of the hard X-ray peaks. This indicates that DPS events are related to the processes of fast energy release and particle acceleration. Furthermore, interpreting DPSs as signatures of plasmoids, we measured their ejection velocity, their width and their height from the DPS spectra, from which we also estimated the reconnection rate and the plasma beta. In this interpretation, constant frequency drift indicates a constant velocity of a plasmoid, and an increasing/decreasing frequency drift indicates a deceleration/acceleration of a plasmoid ejection. The reconnection rate shows a good positive correlation with the plasmoid velocity. Finally we confirmed that some DPS events show plasmoid counterparts in AIA/SDO images.

Subject headings: acceleration of particles — magnetic reconnection — Sun: flares — Sun: particle emission — Sun: radio radiation — Sun: X-rays, gamma rays

[1]National Institute of Information and Communications Technology, 4-2-1, Nukui-Kitamachi, Koganei, Tokyo 184-8795, Japan; nishizuka.naoto@nict.go.jp

[2]Astronomical Institute of the Academy of Sciences of the Czech Republic, 25165 Ondřejov, Czech Republic

[3]Department of Mathematics, University of Dundee, Dundee DD1 4HN, Scotland, United Kingdom

1. Introduction

Various plasma ejections in solar flares are observed in the solar corona. Ejections of soft X-ray emitting plasma blobs and hot loops, i.e. flux ropes in 3 dimensions, are called plasmoid ejections. Plasmoid ejections are observed in multi wavelength emissions: soft X-ray (SXR: e.g. Shibata et al. 1995; Ohyama & Shibata 1997; Tsuneta et al. 1997; Nishizuka et al. 2010), hard X-ray (HXR: e.g. Hudson et al. 2001; Sui et al. 2003; Glesener et al. 2013), UV/EUV (e.g. Liu et al. 2010; Takasao et al. 2012; Kumar & Cho 2013; Liu et al. 2013) and radio emissions (e.g. Kliem et al. 2000; Kundu et al. 2001; Khan et al. 2002; Karlický et al. 2002; Bain et al. 2012). Plasmoids gradually rise up in the preflare phase and are impulsively accelerated in the main phase, in association with HXR bursts. Similarly, when coronal mass ejections (CMEs) are accelerated in the main phase, both HXR bursts and a rapid increase of SXR emission are observed. (CMEs: Zhang et al. 2001; Temmer et al. 2008). Some downward ejections of plasmoids, which collide with the loop-top region, are also reported (Kolomański & Karlický 2007; Liu et al. 2010; Milligan et al. 2010; Takasao et al. 2012). Plasmoid ejections are evidence of magnetic reconnection and multiple X-lines in a solar flare (e.g. Shibata et al. 1995; Ohyama & Shibata 1997; Tsuneta et al. 1997; Karlický 2004; Nishizuka et al. 2010).

Accelerated electrons escaping from the reconnection regions in the upward direction are observed as type III bursts in radio emissions, while downward electron beams are observed as a reverse-drift burst (Aschwanden & Benz 1997). The observed frequency corresponds to the frequency of the plasma surrounding the electron beam, so that electrons propagating in a density gradient of the solar atmosphere show frequency shift in the radio spectra. Having these two bursts interpreted as bi-directional electron beams from one region, we can expect magnetic reconnection or acceleration in that location. Recently it has been shown that acceleration regions exist at several different heights during solar flares, both in observations (Aschwanden 2002; Krucker et al. 2010; Reid et al. 2011) and numerical simulations (Shimizu et al. 2009; Bárta et al. 2011, 2012; Nishida et al. 2013).

Furthermore, some decimetric radio bursts in flares show coherent, quasi-periodic sequences of fast-drifting pulsed structures bound by a pair of slowly drifting low- and high-frequency cutoffs. These are called slowly drift pulsating structures (DPSs: e.g. Kliem et al. 2000; Kundu et al. 2001; Karlický et al. 2002; Khan et al. 2002; Karlický 2004; Karlický et al. 2004; Tan et al. 2007; Tan 2008; Tan et al. 2008; Bárta et al. 2008; Wang et al. 2012). They are caused by quasi-periodic particle acceleration episodes that result from a highly dynamic regime of magnetic reconnection in an extended large-scale current sheet above the SXR loops, where reconnection is dominated by the repeated formation and the subsequent coalescence of plasmoids (Kliem et al. 2000; Karlický 2004; Bárta et al. 2008). Electron

beams trapped in a plasmoid are observed as pulsating structures in a DPS, while the motion of a plasmoid in a density gradient of the solar atmosphere is observed as a global frequency drift.

Electrons are accelerated in a DC field around the X-line in the vicinity of a plasmoid (Karlický & Bárta 2011). The acceleration process of electrons forms an anisotropic velocity distribution, which excites the observed radio emission. The period of DPSs can be explained by the time scale of plasmoids determined by the tearing-mode oscillation (Tan et al. 2007). A few spectra of DPSs are shown to correspond to SXR emitting plasma ejecta (Kliem et al. 2000; Karlický 2004; Tan et al. 2007), in the flare ascending phase just after the onset. Previous studies have shown that all the DPS events are accompanied by GOES SXR flares (Tan et al. 2008), and they occur when the gradient of the GOES SXR curve reaches its maximum (Wang et al. 2012). In our 0.8-4.5 GHz frequency range, most of the DPSs take place at the beginning of the whole flare radio emission, i.e. before the type IV bursts, which is in this range a common flare burst type. From several very broad radio spectra taken by several radiospectrographs, Karlický et al. (2002) found an association of DPSs with type II bursts, generated in the metric radio range by flare shocks. It agrees with the results of Tan et al. (2008) showing a close association of DPSs with CMEs or ejection events.

Plasmoid ejection is strongly related to the reconnection process, as shown in the "plasmoid-induced reconnection model" (Shibata & Tanuma 2001). When we assume an incompressible plasma around a current sheet, the conservation of mass fluxes of the inflow and the outflow leads to the following equation:

$$v_{in} = \frac{W_{pl}}{L_{in}} v_{pl}, \tag{1}$$

where v_{in} is the inflow velocity, L_{in} the length of the inflow region, W_{pl} the width of the plasmoid, and v_{pl} the plasmoid ejection velocity. This equation indicates that the plasmoid ejection induces a reconnection inflow, so that the ejection velocity has a good correlation with the inflow velocity. Even in the case of a compressible plasma, the inflow velocity and the net reconnection rate increase with the plasmoid ejection, when magnetic flux is piled up around a current sheet by the reconnection inflow at the same time as the plasmoid ejection (Ono et al. 2011; Hayashi et al. 2012).

Plasmoid ejections also have an important role in particle acceleration, as well as unsteady impulsive energy release. Current models of particle acceleration during solar flares considering plasmoid dynamics are as follows: (1) DC field acceleration in a reversed X-line between two colliding plasmoids (e.g. Tanaka et al. 2010; Karlický & Bárta 2011), (2) accelerations in a contracting plasmoid after coalescence (Drake et al. 2006; Tanaka et al. 2010; Oka et al. 2010) and in multiple reconnection outflows by interacting plasmoids in 2

dimensions (Hoshino 2012), and (3) acceleration at the fast shock above the loop-top where multiple plasmoids collide (Nishizuka & Shibata 2013). Furthermore, turbulence produced by plasmoid dynamics may couple with stochastic accelerations.

In this paper, we classified DPSs into 4 cases with regards to the plasmoid dynamics, i.e. acceleration/deceleration, and estimated the reconnection rate by using DPSs data. The first advantage of our study is that we analyze 106 DPSs we found during the time period 2002-2012. The number of analyzed DPSs is larger than the previous studies and allows us to statistically study the sample. The second is that, in a gravitationally stratified atmosphere, DPSs show direct information along the vertical direction, i.e. the vertical ejection velocity and not the apparent velocity as usually deduced from imaging observations. The ejection direction is not always vertical, but in many cases the ejection may occur at some angle to the density gradient. This can affect the estimation of the ejection velocity from drift velocities in radio observations, though it would give an error of a factor $\sqrt{2}$ at most when the angle is 45°. The third is that DPSs also contain information about electron beams, which allow us to compare the plasmoid ejection with the particle acceleration. This is why we also compared DPSs and HXR data, and discussed the relationship to the particle acceleration process. Finally we searched for plasmoid counterparts in imaging observations by the Solar Dynamics Observatory (SDO). We explain the analysis method in §2, the analysis results in §3, and we summarize our results and discuss them in §4.

2. Observations of DPS events and their Classification

We used the radio spectrum data taken by the radiospectrograph at the Ondřejov observatory (Jiřička et al. 1993). There are three radio telescopes (RT3, RT4 and RT5) in the frequency range of 0.8-4.5 GHz. The time cadence is 10 ms. The set of data we used covers 11 years from 2002 to 2012. The DPS events between 2002 and 2005 in our paper are partially the same as in a previous paper by Bárta et al. (2008), and we added some events during the same period with a more careful analysis and during 2006 and 2012 with new data (examples in Figures 1 and 2).

During this time period, there are lots of decimetric bursts observed, including type III or reverse-drift bursts and DPSs. The type III or reverse-drift bursts are detached broadband fast-drift bursts, whose typical durations are <1 s. Their origin is interpreted as free electron beams accelerated in the reconnection region. DPSs are ensembles of type III-like bursts, showing coherent, quasi-periodic sequence of fast drifting structures, with pulsed time structures of <1 s, usually bound by a constant or slowly drifting low- and high- frequency cutoffs. The fluctuations of DPSs in time may indicate intermittent energy release or acceleration.

Fast drifting structures inside DPSs, interpreted as trapped particles inside plasmoids, are usually not U-shaped but straight. This is probably because electron beams inside plasmoids lose energy in very short time periods that are less than the circulation time due to the large density. The RT4 and RT5 observing range of 0.8-4.5 GHz corresponds to a plasmoid density of (0.04 - 3)$\times 10^{11}$ cm^{-3}. Interpreting DPSs as signatures of plasmoids, the drifts towards lower/higher frequencies mean upward/downward motions of plasmoids. The DPSs with decreasing/increasing frequency drifts mean acceleration/deceleration of plasmoids.

In this paper, we found 106 DPS events during 2002-2012. We dealt with multiple DPS events in a single flare as a single event, though Bárta et al. (2008) counted every DPSs as individual events. This is why the number of DPS events in Bárta et al. (2008) looks larger, although the number of DPSs we analyzed is much larger than in their paper. We summarized the events in Table 1, where we noted some characteristics of these DPSs. Some DPSs drift to lower frequencies, and others drift to higher frequencies or have no drift. The frequency drift sometimes varies in time. Some DPSs oscillate around a certain frequency. Most of the DPSs occurred at the beginning of the impulsive phase of flares and sometimes of the radio bursts known as broadband continuum (type IV burst), which is consistent with Tan, C. et al. (2008). Sometimes they appear after the impulsive or main phase, and small numbers of events are not associated with flares (inconsistent with Tang et al. 2007; this is discussed in detail in §3).

First, we determine the background-subtracted radio spectra in the 0.8-4.5 GHz range and measure the start and end times, t_{start} and t_{end}. We also measure the low- and high-frequency cutoffs of every decimetric bursts, listed as f_{max} and f_{min}, at the start of the event as well as the end time (see Fig. 2). The upper/lower edge of the DPS is determined by eye. We determine the duration as Δt=$t_{end} - t_{start}$. It is noted that the frequency drift rate changes in quite a short time period <100 ms, as shown in Figure 2, so that the frequency drift rate shows discontinuity during the acceleration and in each period the frequency drift rate can be well fitted by a linear approximation (cases (III) and (IV) in the next paragraph). When a DPS event shows changes in the frequency drift rate, we separate the event to shorter periods with an approximately constant frequency drift and measure t_{start}, t_{end}, f_{max} and f_{min} for each period.

Following the different characteristics of DPSs, we classified our 106 DPS events into four categories: (I) single DPS events with a constant frequency drift (drift towards lower or higher frequencies), (II) multiple DPS events occurring in the same flare with constant frequency drifts, (III) single or multiple events with increasing or decreasing frequency drift rates and (IV) complex events containing multiple events occurring at the same time in the different frequency range. Cases (I) and (II) have only three events with no frequency drift,

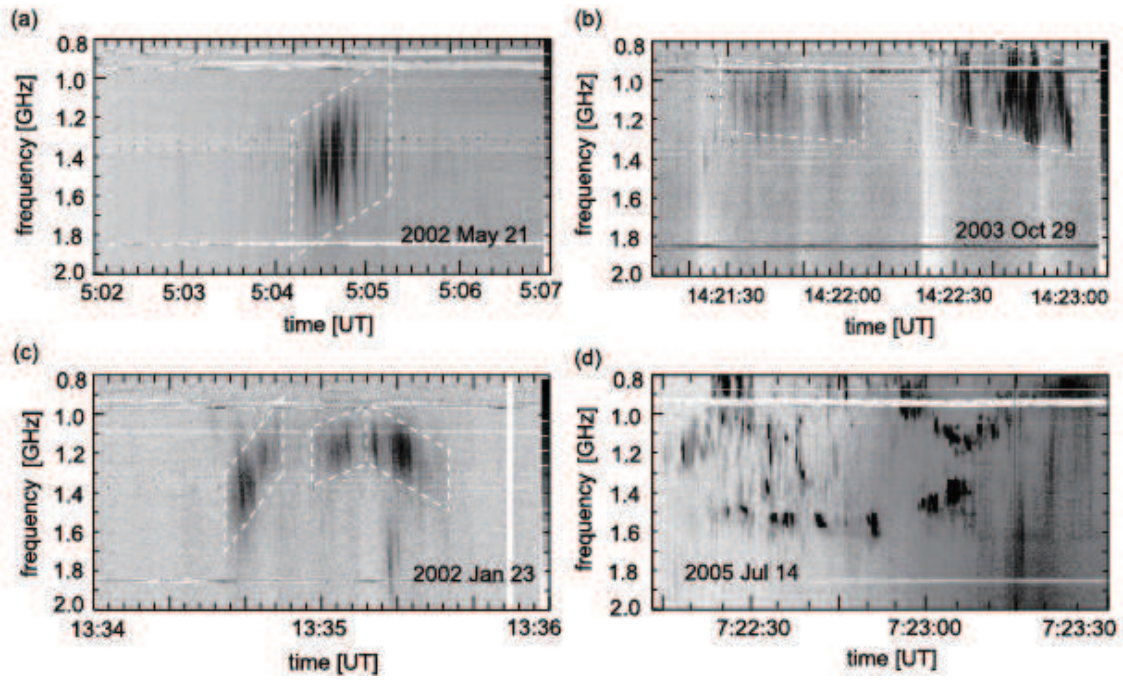

Fig. 1.— Typical DPS events taken by Ondřejov radiospectrograph telescopes: (a) (I) single events with constant frequency drift, (b) (II) multiple events with constant frequency drifts, (c) (III) single event or multiple events with increasing/decreasing frequency drift rates and (d) (IV) complex events including multiple events occurring at the same time in the different frequency range.

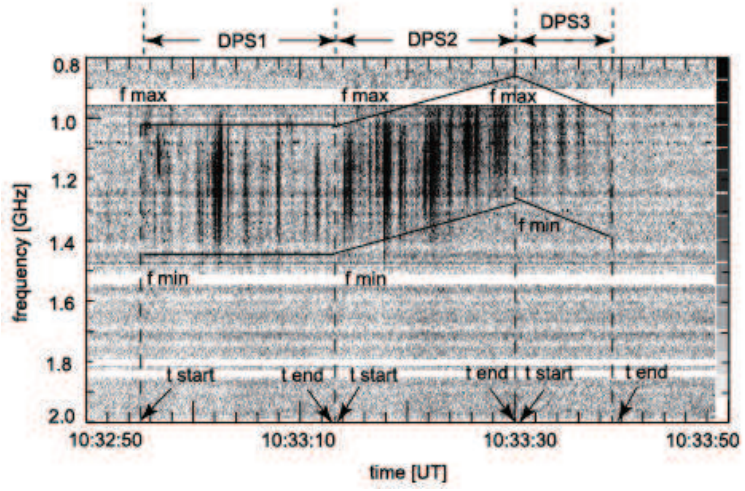

Fig. 2.— A typical DPS event (case (III)) taken by Ondřejov radiospectrograph telescope on 2011 Mar 6 with the measurable parameters indicated.

whereas cases (III) and (IV) include lots of events with no frequency drift preceding/following the acceleration/deceleration. The number of events for case (I) is 12 events, 11 events for case (II), 52 events for case (III) and 31 events for case (IV). This leads to the fact that case (III) is the most common and case (IV) is the second. Therefore, DPSs usually have increasing or decreasing frequency drift rates. Those different categories are illustrated in Figure 1.

The motions of the DPSs in case (III) have typically three patterns: no drift to drift towards lower frequency, drift towards higher frequency to no drift, and drift towards higher frequency - no drift - drift towards lower frequency. It seems that most of the DPSs in case (III) tend to decrease the frequency drift rate. The initial frequency and the frequency drift rate of DPSs in case (II) are random. The patterns of the DPSs in case (IV) are sometimes very complex, composed by multiple DPSs with increasing/decreasing frequency drifts. Some of them are superposed and seem to be merged or split. Multiple DPSs appear at the same time in different frequency ranges. The observation of multiple DPSs may indicate multiple plasmoids formed in a current sheet via the secondary tearing mode instability, which leads to the repetition of the coalescence process and bursty ejections.

Figure 3 shows the year variation of the number of detected DPS events during 2002-2012. The first peak is around 2002, and the second one is in 2012. During 2006-2009, no DPSs were observed, except for one event in 2007. This seems to correspond with the 11-year period of solar activity variation. Especially case (III) shows the most sensitive and dramatic changes along the solar activity.

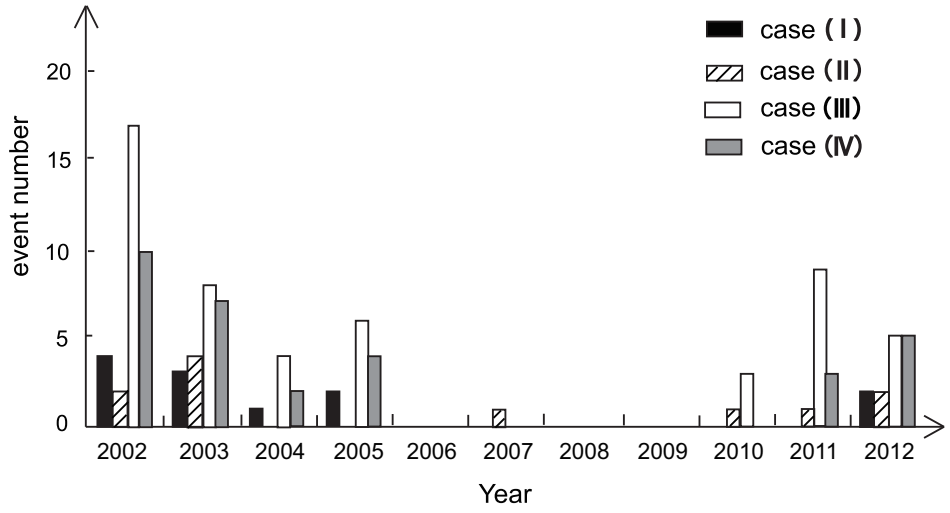

Fig. 3.— Year variation of the number of DPS events during 2002-2012, with DPSs classified in four different categories.

Table 1. Event list of the 106 DPS events during 2002-2012.

Date[a]	Time[b]	Case[c]	RHESSI[d]	GOES[e]	Date[a]	Time[b]	Case[c]	RHESSI[d]	GOES[e]
2002/04/04	15:27:40	I	○	-	2002/05/17	07:37:40	I	○	-
2002/05/21	05:04:10	I	-	○	2002/08/30	13:27:37	I	○	-
2002/11/14	11:09:26	I	○	-	2003/01/26	10:28:55	I	-	○
2003/05/27	06:42:43	I	-	○	2003/05/30	08:51:55	I	-	○
2005/01/13	11:25:32	I	○	-	2005/06/14	07:21:40	I	-	○
2012/07/06	08:46:21	I	-	×	2012/07/11	08:27:04	I	-	○
2002/07/11	14:46:00	II	○	-	2002/11/10	08:47:36	II	○	-
2003/06/02	08:29:05	II	-	○	2003/10/20	07:09:54	II	○	-
2003/10/29	14:21:30	II	-	○	2003/11/11	13:40:30	II	-	○
2007/01/10	09:50:13	II	-	○	2010/02/12	11:24:09	II	○	-
2011/10/01	12:37:35	II	○	-	2012/04/25†	08:56:00	II	○	-
2012/07/06	06:14:02	II	○	-					
2002/01/23	13:34:36	III	-	○	2002/02/07	13:36:04	III	-	○
2002/04/10	12:27:45	III	○	-	2002/05/07*	14:08:33	III	-	×
2002/05/20	15:25:03	III	-	○	2002/06/30	11:01:13	III	○	-
2002/08/30*	13:38:45	III	×	-	2002/08/30	14:36:35	III	-	○
2002/08/31	10:01:27	III	-	○	2002/08/31	13:52:16	III	-	○
2002/08/31	14:20:25	III	○	-	2002/09/01	12:13:55	III	-	○
2002/09/05	16:24:55	III	○	-	2002/09/20	12:37:33	III	○	-
2002/09/21	07:58:04	III	○	-	2002/09/29	06:38:40	III	○	-
2002/10/14	09:29:22	III	-	○	2003/03/18	12:04:00	III	○	-
2003/04/30†	07:30:14	III	○	-	2003/05/27†	08:01:20	III	○	-
2003/06/02†	09:43:45	III	○	-	2003/06/09	10:46:16	III	-	○
2003/06/10	08:35:35	III	-	○	2003/10/25	12:15:52	III	-	○
2003/11/18	08:23:10	III	○	-	2004/07/23	06:43:42	III	○	-
2004/07/23	17:19:06	III	-	○	2004/07/25	15:05:00	III	○	-
2004/10/30	10:26:10	III	○	-	2005/05/05	14:25:55	III	○	-
2005/05/09	09:55:40	III	-	○	2005/05/10	09:30:32	III	○	-
2005/05/11†	15:35:07	III	○	-	2005/07/12	08:08:50	III	○	-
2005/09/13	11:20:36	III	○	-	2010/02/12	11:22:00	III	○	-
2010/06/13	05:35:00	III	○	-	2010/07/30†	11:08:50	III	○	-
2011/01/21	10:50:32	III	-	○	2011/02/19	08:03:50	III	○	-
2011/03/06	10:32:55	III	-	○	2011/05/28	11:16:11	III	-	○

Table 1—Continued

2011/08/02	11:37:56	III	○	-	2011/08/08	12:16:22	III	○	-
2011/08/08	15:34:47	III	○	-	2011/08/08	15:56:24	III	-	○
2011/12/21	11:03:44	III	○	-	2012/05/08	13:04:42	III	-	○
2012/05/09	10:26:21	III	-	○	2012/06/13	12:50:04	III	-	○
2012/07/04	14:39:46	III	-	○	2012/07/12	14:16:06	III	-	○
2002/03/16	11:22:20	IV	-	○	2002/04/10	06:56:26	IV	-	×
2002/06/02	10:44:40	IV	×	-	2002/08/17	14:36:30	IV	○	-
2002/08/20	14:28:30	IV	-	○	2002/08/29	12:46:50	IV	-	○
2002/09/17	09:17:02	IV	○	-	2002/09/28	10:34:40	IV	-	○
2002/11/21	12:43:18	IV	○	-	2002/11/25	10:41:49	IV	○	-
2003/01/03†	13:25:27	IV	○	-	2003/02/14	09:16:06	IV	○	-
2003/05/28*	08:08:24	IV	×	-	2003/06/09	16:27:01	IV	○	-
2003/06/10	16:29:30	IV	○	-	2003/06/11	09:55:30	IV	-	○
2003/11/17	09:20:10	IV	-	×	2004/01/08*	10:27:18	IV	-	×
2004/10/30	13:46:55	IV	○	-	2005/05/09	11:28:56	IV	-	○
2005/06/14	07:52:27	IV	×	-	2005/07/11	16:35:20	IV	-	○
2005/07/14	07:22:19	IV	-	○	2011/05/29	09:45:45	IV	-	○
2011/09/24*	15:12:35	IV	-	×	2011/10/13	14:50:22	IV	-	○
2012/01/14	13:15:50	IV	-	○	2012/07/03	13:57:48	IV	-	○
2012/07/03	17:00:18	IV	×	-	2012/07/06	07:05:48	IV	-	○
2012/07/06	13:29:25	IV	-	○					

Note. — [a]Date (yyyy/mm/dd), [b]Start time [UT], [c]Classification: case (I)-(IV), [d]RHESSI peak (with/without ○/×; no data −), [e]GOES time derivative peak (with/without ○/×, events with RHESSI data are skipped −). Here we consider events occurring during different flares. † mark denotes the events with HXR peaks but without GOES SXR flares. ∗ mark denotes the events with neither HXR nor GOES SXR flares.

3. DPSs in association with HXR bursts

3.1. Measurements of HXR peaks

DPSs are ensembles of type III-like bursts, i.e. emissions from high energy electron beams via wave-particle interactions. In DPSs, electrons are trapped in plasmoids. Therefore these trapped electrons cannot reach dense layers of the solar atmosphere where the X-rays are usually generated, i.e. the chromosphere and the photosphere. However, there are electrons accelerated simultaneously in the same reconnection region, which are not trapped in the plasmoids. These can then generate HXRs in deep and dense layers of the Sun's atmosphere. Therefore, some association of DPSs and HXR bursts can be expected (Karlický et al. 2004). This association can be further influenced by the fact that any beam of superthermal electrons generate the X-rays in dense layers, but the radio emission of the beam can be reduced due to an inappropriate beam distribution function, reduced wave conversion, and absorption effects. On the other hand, if the magnetic field structure associated with many interacting plasmoids becomes complicated, all accelerated electrons are trapped in this structure and do not reach the dense layers of the solar atmosphere. In this case we can observe DPSs without corresponding HXRs. Since a DPS (a series of acceleration episode) lasts much longer than a single type III bursts (one acceleration episode), we study here the mean association of DPSs with HXR peaks, i. e. not for individual acceleration episodes as in the analysis of type III bursts and HXR peaks (Benz et al. 2005).

To compare DPS events with HXRs, we used data taken by RHESSI (Lin et al. 2002), whose time cadence is 4 s. We checked all the RHESSI data for the 106 DPSs presented above, and 51% of all events (54 DPSs) turned out to be simultaneously observed with RHESSI. For these events, we drew light curves integrated on-disk in three different energy ranges, 15-25 keV, 25-50 keV and 50-100 keV. For one DPS event not correlated with any RHESSI data, we used data taken by the Czech-made Hard X-Ray Spectrometer (HXRS Fárník et al. 2001) onboard the U.S. Department of Energy Multispectral Thermal Imager satellite (MTI). HXRS has three energy bands: HXRS-S1 for 19-29 keV, HXRS-S2 for 44-67 keV and HXRS-S3 for 100-147 keV, with a time cadence of 200 ms. For the other events with neither RHESSI nor HXRS data, we calculated the time derivative of SXR light curves taken by GOES, whose peak is believed to be well correlated with HXR peaks, as known from the Neupert effect (1968). The criterion used to distinguish whether there is a HXR component is an evident increase of HXR emission up to over 40 counts with 4 s cadence (above the background level) in a short time scale, at least in an energy band of 15-25, 25-50, or 50-100 keV. As for the events without RHESSI HXR data, we picked up all the events with positive GOES SXR gradients occurring at the same time as DPSs.

3.2. Coincidence of DPS events and HXR/SXR flares

We find that 49 DPSs events (90%) with RHESSI are associated with HXR peaks, and 5 events (10%) are not (Table 2). When considering all the events with RHESSI, HXRS or GOES, we found that 95 events (90%) are correlated with HXR peaks and/or SXR peak gradients, and 11 events (10%) are not (Table 3). We summarize the results also in pie graphs of Figure 4, which indicates that most of the DPS events are related to HXR emissions and are associated with particle acceleration. Moreover, we also find that more than 90% of case (I)-(III) events are correlated with HXR peaks, whereas case (IV) shows only 74% of HXR events. In other words, not all the DPS events are associated with HXR events. Especially case (IV) is less correlated with HXR peaks. Considering Neupert effect (1968), it can be rewritten that not all the DPS events are in association with SXR flares.

Actually we confirmed that not all the DPS events are correlated with GOES SXR flares over C-class. Majority of DPSs occurred with HXR and SXR flares, but some DPSs with SXR flares and no HXRs (indicating soft flares), some (7 DPS events, attached with † mark in Table 1) with HXRs but without SXRs (because the count of HXRs is so small like 40-200 that the SXR component is covered in SXR background), and the others (5 DPS events with $*$ mark in Table 1) with neither HXRs nor SXRs (but these were also in active regions). For the last 12 events without SXR flares, seven of them are interpreted as independent events from SXR, because the time difference between DPSs and SXR peaks is so large. Two of them occurred in decay phase of GOES flares without any enhancement of SXR. One is in the quiet SXR activity. Three of them are neglected because of the small increase of SXR like from GOES C5.0 to C5.4. These are probably because the magnetic structure in Case (IV) is complex, which can trap in some cases all accelerated electrons, and thus no accelerated electrons reach dense layers of the solar atmosphere, and then much reduced X-ray emission is produced.

Figures 5-7 show typical DPS events associated with HXR bursts. The radiospectra of DPSs are attached with HXR light curves taken by RHESSI, with solid line (15-25 keV), dotted line (25-50 keV) and dashed line (50-100 keV). Every event shows an evident emission in the energy band 15-25 keV, but only a small number of events show very weak ones in higher energy bands. This indicates that DPSs are more related to particles/plasmas in the energy range of 15-25 keV, rather than in the higher energy range of 25-100 keV. The occurrence ratio of different HXRs energy events is summarized in Table 4. All the DPSs associated with HXR peaks taken by RHESSI are accompanied by an enhancement in the 15-25 keV band. HXRs in the 25-100 keV bands are observed in less than 25% of all the events which were associated with HXRs in the 15-25 keV range. Case (I) shows the largest occurrence ratio of 50-100 keV events to 15-25 keV events, case (IV) show the second, case

(II) the third and case (III) shows the smallest.

HXR light curves sometimes show a small hump before the main peak in time, which is well correlated with a DPS event. It is also noted that HXRs in different energy bands show time difference between their peaks, i.e. higher energy peaks are reached earlier than lower energy peaks, and DPSs are in general more closely correlated with the higher energy peaks in terms of the timing, only when there is a HXR peak in higher energy bands. This can be explained as higher energy particles can precipitate to the chromosphere faster than lower energy ones, so the timing of higher energy particles is closer to the timing of particle acceleration in the corona near DPS-emitting plasmoids.

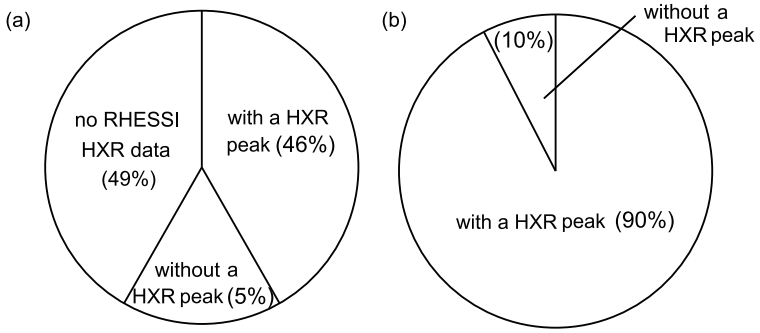

Fig. 4.— (a) The percentage of DPS associated with a HXR peak observed by RHESSI or HXRS. "Without a HXR peak" means that there were no HXRs observed above the background level. "No RHESSI HXR data" means no RHESSI data during DPS events. (b) The same as (a) using the time derivative of the GOES SXR flux for "no RHESSI" events.

Table 2. The number of events with or without HXR peaks for each case (I)-(IV). HXR data is taken by RHESSI and HXRS.

	case (I)	case (II)	case (III)	case (IV)	Total
with HXR peaks	5	7	28	9	49
no HXR peaks	0	0	1	4	5
no RHESSI data	7	4	23	18	52
Total	12	11	52	31	106

Table 3. The number of events with or without HXR peaks or GOES SXR gradient peaks for each case (I)-(IV). HXR data is taken by RHESSI and HXRS.

	case (I)	case (II)	case (III)	case (IV)	Total
with HXR/SXR grad. peaks	11	11	50	23	95
no HXR/SXR grad peaks	1	0	2	8	11
Total	12	11	52	31	106

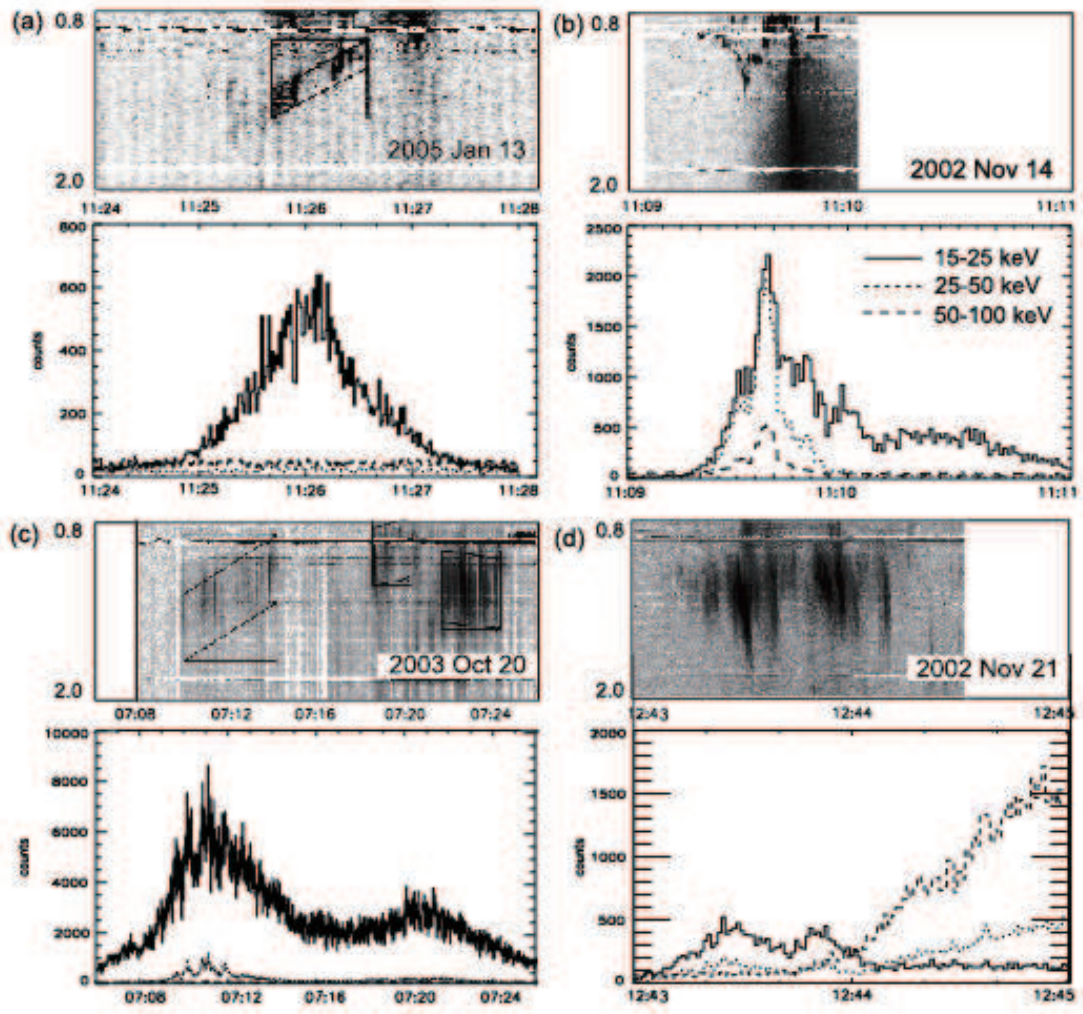

Fig. 5.— Typical DPS events taken by radiospectrograph telescopes in Ondřejov observatory and HXR light curves taken by RHESSI in different energy ranges (15-25, 25-50, and 50-100 keV). (a)-(d) show events with $\Delta t<0$, where $\Delta t=t_{DPS}-t_{HXR}$. Furthermore, (a) has no HXR>25 keV, (b) HXR<25 keV coincides with HXR>25 keV, (c) HXR<25 keV coincides with HXR>25 keV and HXR peak is long, (d) HXR<25 keV precedes HXR>25 keV.

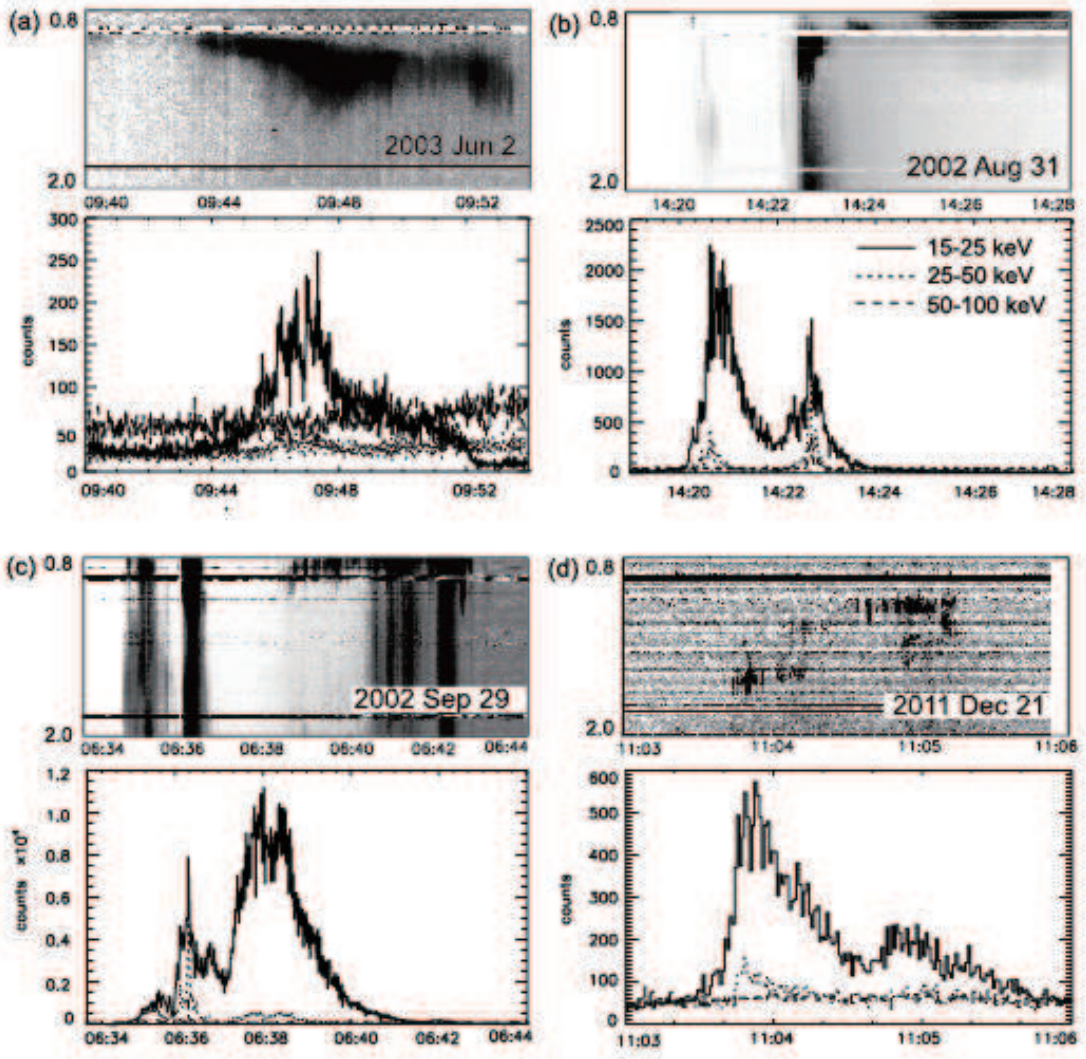

Fig. 6.— Comparison between DPSs observed in Ondřejov observatory and HXRs observed by RHESSI in different energy ranges (15-25, 25-50, and 50-100 keV): (a) Δt=0 and no HXR>25 keV, (b) Δt=0 and HXR<25 keV coincides with HXR>25 keV. (c) Δt>0 and HXR<25 keV coincides with HXR>25 keV. (d) Δt>0 and HXR<25 keV precedes HXR>25 keV. Here $\Delta t = t_{DPS} - t_{HXR}$.

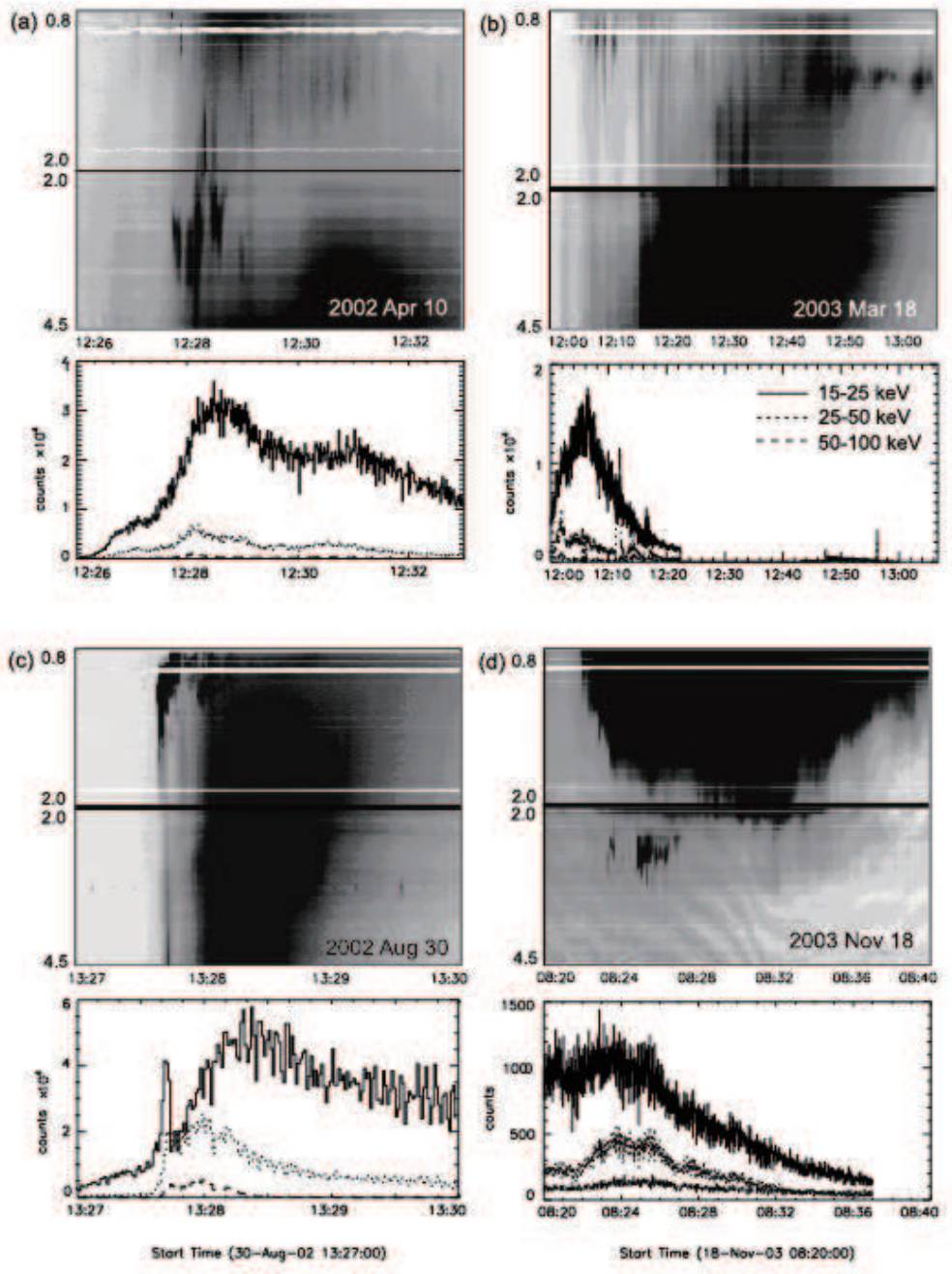

Fig. 7.— DPS events with radio bursts known as broadband continua (or type IV burst) and HXRs observed by RHESSI in different energy ranges (15-25, 25-50, and 50-100 keV): (a)-(c) Δt=0 and $f_{DPS} < f_{burst}$. (d) Δt>0 and $f_{DPS} > f_{burst}$. Here Δt=t_{DPS}-t_{HXR}.

3.3. Time difference between DPSs and HXR peaks

DPS events (with HXR peaks) can be classified by their relation with these peaks. Figure 5 shows events which precedes HXR peaks. Figure 6(a)-6(b) shows DPSs whose acceleration or deceleration occur at the same time as HXR peaks, and Figure 6(c)-6(d) shows events delayed to HXR peaks. Here we determine the peak time of HXR (15-25 keV), t_{HXR}, and the start time of the corresponding DPSs, t_{DPS}. The time difference between the two times (Δt=t_{DPS}-t_{HXR}) is illustrated in Figure 8. A positive Δt corresponds to a delay of DPSs relative to HXR, while a negative Δt indicates the occurrence of DPSs before the onset or during the rising phase of HXR bursts. In Figure 9, most of the events are distributed in the range of -60 s< Δt <30 s, which can be fitted with a Gaussian function centered at the null value for Δt, and with its negative-side tail enhanced (or double Gaussian functions are also suitable). This means that DPSs mainly occur in the flare ascending phase just after the onset of the flare, and that DPSs occur when the gradient of SXRs reaches the maximum (see also Wang et al. 2012). There are minor extreme events with $|\Delta t|$ >60 s, but these may be independent from the HXR activity. Furthermore, there is no tendency that the events with larger/smaller Δt are associated with larger/shorter duration HXR peaks, i.e. when Δt is small the events are not always impulsive.

As explained above, the association of DPSs with HXRs can be influenced by the radio emission mechanism and by the trapping in the complex magnetic fields resulting from the formation, and possibly the interaction, of multiple plasmoids. The acceleration regions in the current sheet higher in the corona can get magnetically connected and/or disconnected multiple times, as the magnetic topology evolves in the layers below (see e.g. Bárta et al. 2011). Namely, new plasmoid formation and coalescence, taking place below the acceleration region influences the evolution of the magnetic connectivity of this acceleration region all the way down to the chromosphere/photosphere. Therefore, defining a clear correspondence between the radio DPS emissions and HXR remains difficult. Here we propose to look at general tendencies for this connection that can be deduced from observations. We interpret cases of positive Δt when the radio emission takes more time, for radiation process to take place, e.g. specific velocity distribution, than HXRs. Cases with negative Δt may indicate that the trapping in a complex magnetic field or complex magnetic connectivity domain leads to particles necessitating more time to precipitate to the chromosphere due to the trapping in the magnetic topology, or that very few high energy particles first escaped to the lower dense layers, leading to weak HXRs, while the bulk of high energy particles emitting HXRs escaped with a slight delay.

The enhancement of HXRs during the acceleration of a plasmoid is only evident for one event. Rather, during multiple plasmoid acceleration events or multiple DPS events,

initially enhanced HXR emission gradually decreases (28 events, e.g. Fig. 5(c)) or reaches the background level (5 events, e.g. Fig. 6(a)). When the HXR curve has multiple enhancements, some DPSs also have multiple enhancements in the intensity of the radio/microwave emission (e.g. Figs. 5(d) and 6(d)).

Figure 7 shows DPS events with additional radio bursts which are called broadband continuum or type IV burst. 6 events out of the 48 DPS events with RHESSI HXR peaks are accompanied with radio bursts in the frequency range of 0.8-4.5 GHz. 1 event occurred during the main phase of the radio burst, while 5 events occurred before or at the initial phase of the radio burst. It is also noted that one DPS during the main phase is observed in the higher frequency of a radio burst, while 5 DPSs before radio bursts are in the lower frequency. Tan et al. (2008) reported that 88% of DPSs took place at the initial phase of radio bursts (0.6-7.6 GHz) in their analysis. In our analysis, DPSs with radio bursts known as the broadband continuum (type IV burst) only represent 13% of all the cases, and 5/6 (=83%) of the events occurred at the initial phase of the radio bursts. Fárník et al. (2001) also reported that the GHz broadband radio pulses taken by the 3 GHz Ondřejov radiometer are delayed by 2-14 s related to the HXR emission peaks. If DPSs are synchronized with HXR peaks, DPSs should be observed 2-14 s prior to the radio bursts.

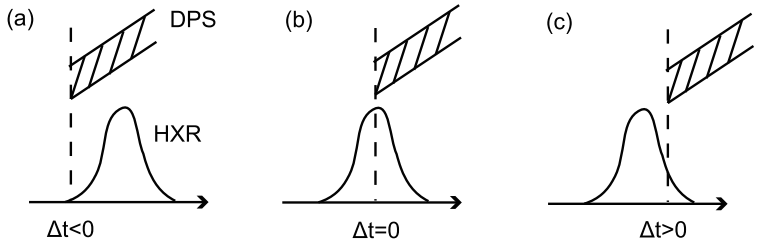

Fig. 8.— The relationship between the start time of a DPS and the peak time of HXRs: (a) DPS precedes HXR, (b) DPS and HXR occur at the same time, (c) DPS is delayed with HXR. Here $\Delta t = t_{DPS} - t_{HXR}$.

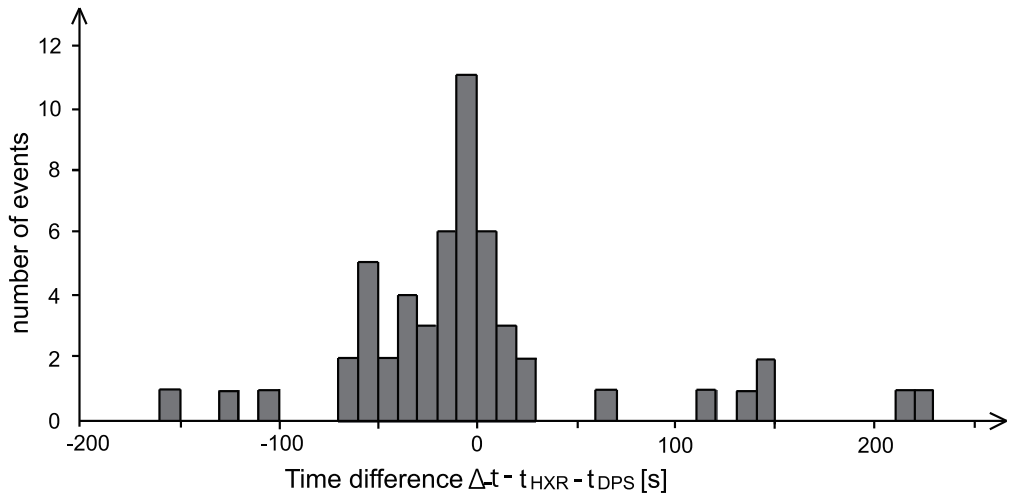

Fig. 9.— Histogram of the time difference between the peak time of HXRs and the start time of an isolated DPS or a series of multiple DPSs.

Table 4. Distribution of DPS events observed with HXRs from the RHESSI data, for different energy ranges.

	Low Energy (15-25 keV)	Middle Energy (25-50 keV)	High Energy (50-100 keV)
Case (I)	5	3	2
Case (II)	7	3	2
Case (III)	27	14	5
Case (IV)	8	5	3
Total	47	25	12
	(1.00)	(0.53)	(0.25)

4. Statistical Results for the Characteristics of Plasmoids

4.1. Basic equations, and Derivation of the Plasmoid properties

It has long been established that fast-drifting radio bursts (type III and reverse-drift bursts) in the decimetric frequency range are caused by radiation from plasma oscillations excited by electron beams (Wild et al. 1954), with typical exciter velocities of v_b/c=0.07-0.25 (Dulk et al. 1987). Similarly, in DPSs the fast drifting features were proposed to be generated by the plasma emission mechanism with electron beams (Kliem et al. 2000). With this assumption, in the next step, we convert the measured radio frequencies f_{max} and f_{min} into approximated values of electron densities, i.e. n_{max} and n_{min}, by setting the observed radio frequency equal to the fundamental electron plasma frequency f_p,

$$f_p = 8980\sqrt{n_e} \tag{2}$$

with n_e the electron density (in cgs units). Implicitly it is assumed that the observed decimetric radio emission is related to the fundamental plasma emission. If some bursts were emitted at the harmonic level of the plasma frequency, the inferred density would be a factor 4 lower.

Here we link the atmospheric density with the magnetic field strength, the height of the DPS event, etc. First, the plasma density in the environment surrounding the plasmoid, noted hereafter n_{out}, is given by models from Alvarez & Haddock (1973) and Aschwanden & Benz (1997) (see also Equation 176 in Aschwanden 2002),

$$n_{out}(h) = \begin{cases} n_1 \left(\frac{h_1}{h}\right)^p & (h \le h_1), \\ n_Q \exp\left(-\frac{h}{\lambda_T}\right) & (h \ge h_1) \end{cases} \tag{3}$$

where h_1=1.6×10^{10} cm is the transition height between the lower and the higher corona, n_1=4.6×10^7, cm^{-3}, n$_Q$=4.6×10^8 cm^{-3} is the base density, $\lambda_T = RT/g$=6.9×10^9 cm is the thermal spatial scale of density, and the power-law index is p=2.38. We can estimate the coronal magnetic field by considering the Sun as a magnetic spherical dipole, as suggested in Aschwanden (1999),

$$B_{cor}(h) = B_0 \left(1 + \frac{h}{h_D}\right)^{-3} \tag{4}$$

where B_0=100 G and h_D=7.5×10^9 cm. It is noted here that, for the purpose of our study, we need some simple formula approximating the dependence of the magnetic field on heights in the corona. In the review book of Aschwanden (2004) (page 19-20), there are two such approximations: the Dulk and McLean's formula which is valid above $1.02R_{sun}$ (Dulk & McLean 1978) and the Aschwanden's approximation. Both approximations were

derived from observations. We used the Aschwanden's approximation, because it is a commonly used approximation of the magnetic field in the low corona. It is true that the current layer where the plasmoids are formed is quite a complex region, however, even in simulations of plasmoid formation, the ambient magnetic field around the current sheet is often considered to be simple (for example, with a single shearing layer such as often considered Harris sheets). As such, since we are mostly interested in the large-scale property of the magnetic field in the region surrounding the plasmoid, taking a simple model for the coronal field such as Aschwanden's one should still be a valid approximation.

Furthermore, when the gas pressure inside a plasmoid balances with the gas pressure and the magnetic pressure outside of the plasmoid, the following relationship is satisfied,

$$2n_{in}(h)k_BT_{in} = 2n_{out}(h)k_BT_{out} + \frac{B_{cor}^2(h)}{8\pi} \tag{5}$$

This equation is rewritten as follows,

$$n_{in}(h) = n_{out}(h)\frac{T_{out}}{T_{in}} + \frac{B_{cor}^2(h)}{8\pi}\frac{1}{2k_BT_{in}} \tag{6}$$

Here we neglected the term of magnetic pressure, i.e. the guide field, inside a plasmoid for simplicity. If the guide field inside a plasmoid is not negligible, n_{in} is overestimated and gives the upper limit. By inserting the equations above (2)-(4) to this pressure balance equation (6), we get the following equation,

$$n_{in}(h) = \begin{cases} n_1 \left(\frac{h_1}{h}\right)^p \frac{T_{out}}{T_{in}} + \frac{B_0^2}{8\pi 2k_BT_{in}} \left(1+\frac{h}{h_D}\right)^{-6} & (h \le h_1) \\ n_Q \exp\left(-\frac{h}{\lambda_T}\right) \frac{T_{out}}{T_{in}} + \frac{B_0^2}{8\pi 2k_BT_{in}} \left(1+\frac{h}{h_D}\right)^{-6} & (h \ge h_1) \end{cases} \tag{7}$$

Here the temperatures in the corona and surrounding the plasmoid, and in the plasmoid itself, are supposed to be constant. These assumptions can be made since the time scale of the thermal conduction t_{cond} is much shorter than the typical time scale τ. Referring to Ohyama & Shibata (1998) and Nishizuka et al. (2010), we set the coronal temperature T_{cor}=1.5×10^6 K, and the plasmoid temperature T_{in}=1.0×10^7 K.

From equation (6), we have obtained a direct relation between the density inside the plasmoid, n_{in}, and the height of the DPS emission. By using f_{max} and f_{min}, deduced from the observations at the start of the DPS event, we can calculate the related n_{max} and n_{min} with equation (2), and deduce the heights h_{min} and h_{max} that give the size of the plasmoid W_{pla}=h_{max}-h_{min} (Fig. 10). Here we assume that the plasmoid is of a similar extent in width as in height. In the following, we also define the average height of the plasmoid at the start time h_{start}= (h_{max}+h_{min})/2 as well as h_{end} for the end of the event.

Then, the other plasmoid properties can be computed as follows. The plasmoid ejection velocity is given as the difference during Δt of the average heights of the plasmoid,

$$v_{pla} = \frac{\Delta h}{\Delta t} = \frac{h_{end} - h_{start}}{t_{end} - t_{start}} \tag{8}$$

The Alfvén speed and the plasma β, the ratio between thermal and magnetic pressures, are calculated from the outside coronal magnetic field and density,

$$v_A(h) = \frac{B_{cor}(h)}{4\pi m_p n_{out}(h)} \tag{9}$$

$$\beta = \frac{2n_{out}(h)k_B T_{out}}{B_{cor}^2(h)/8\pi} \tag{10}$$

Assuming an incompressible plasma in the reconnection region (such as Sweet-Parker reconnection model), the reconnection rate M_A is expressed by the mass conservation equation between the inflow and the outflow: $v_{in}L_{in}= v_{pla}W_{pla}$ (equation (1); see also Shibata & Tanuma 2001). Then, the reconnection rate, calculated with the normalized inflow velocity, as well as the energy release rate, are given as follows,

$$M_A = \frac{v_{in}}{v_A} = \frac{W_{pla}}{L_{in}} \cdot \frac{v_{pla}}{v_A} \tag{11}$$

$$\frac{dE}{dt} = 2\frac{B_{cor}(h)^2}{4\pi} v_{in} L_{in}^2 \tag{12}$$

In the following, we assume that L_{in} is similar to the height of the DPS emission at the start of the event, h_{start} (Fig. 10). This is acceptable, when the length of a current sheet is much larger than the height of the loop-top (L_{in}=h_{start}-$h_{loop-top}$-$\frac{W_{pla}}{2}$ $\sim$ h_{start}). On the basis of our calculation result (Fig. 11 in the next section), it is true that the estimated height of the plasmoid is (2-4)$\times 10^9$ cm, which is larger than the typical loop-height ($\sim 10^9$ cm). Some EUV observations of plasmoid ejection show that the current sheet can extend much further above the flare loops (e.g. Lin & Forbes 2000; Webb et al. 2003; Savage et al. 2010; Reeves & Golub 2011). However, in cases considered here with DPS events associated with HXR peaks and therefore occurring in the impulsive phase at the start of the flare, the current sheet is expected much shorter than several R_{sun} what Savage et al. (2010) find several hours after the loss of equilibrium. At the time of the DPS, the flare loops could account for 50% of the calculated plasmoid height. L_{in} also includes the added radius of the plasmoid at the top of the current sheet. The uncertainties of this L_{in} propagate through to the determination of the reconnection rate M_A in the following equation;

$$\frac{|\Delta M_A|}{M_A} = \frac{|\Delta W_{pla}|}{W_{pla}} + \frac{|\Delta L_{in}|}{L_{in}} + \frac{|\Delta v_{pla}|}{v_{pla}} + \frac{|\Delta v_A|}{v_A} \tag{13}$$

Therefore, the uncertainty of M_A is also 50-90% from the determination and measurement errors of L_{in}, in addition to the errors from the other parameters.

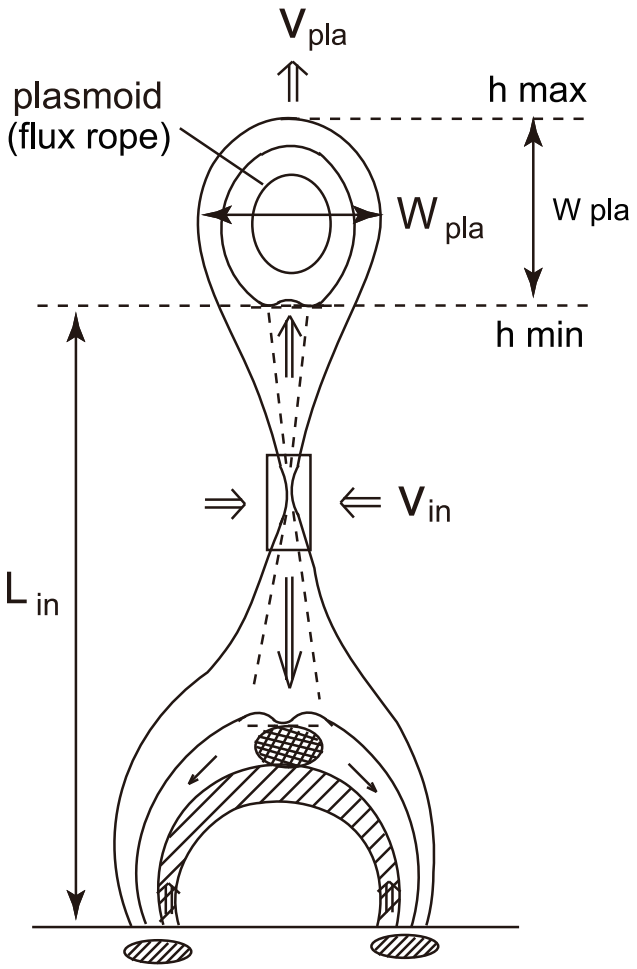

Fig. 10.— Cartoon of a flare eruption with the plasmoid ejection velocity v_{pla}, the width of a plasmoid W_{pla}, the length of the inflow region L_{in} and the inflow velocity v_{in}.

4.2. Distributions of Velocity, Width, Height of Plasmoids and Reconnection Rate: Case (I)+(II) and (III)

Figure 11 shows histograms of the distribution of the velocity, the width, the height of ejected plasmoid and the reconnection rate, which are calculated from the DPS events of cases (I)+(II) and (III). We consider cases (I) and (II) together as they have a similar definition (events with constant frequency drifts) and as to allow direct comparison with the more numerous DPSs of case (III). We also do not show the histograms for case (IV)-DPSs, as these events are rather complicated with multiple events with non-constant frequency drifts happening at the same time: the histogram would be biased by how we would separate each individual event.

Interpreting DPSs as signatures of plasmoids, most of the cases (I)+(II)-events show upward motions of plasmoids, while the case (III)-events contain both upward and downward plasmoid events. The case (III)-events show acceleration or deceleration of plasmoids and velocity change in time. The two phases before and after acceleration/deceleration are counted twice in case (III) and events with n-times velocity changes are counted (n+1) times, similar to Bárta et al. (2008). The velocity of plasmoids is mainly in the range of 0-5$\times$ 10^7 cm s^{-1} (Fig. 11(a)). The 60-70% of case (III) are upward events, while 30-40% are downward events. The distributions of upward and downward events are almost the same. The width of a plasmoid is typically (0.3-1.1)$\times 10^9$ cm, and the height of the plasmoid, i.e. the length of a current sheet attached below the plasmoid, is typically (1.8-3.6)$\times$ 10^9 cm (see Figs. 11(b)-11(c)). This is the first paper to estimate the width of the plasmoid and the length of a current sheet (W_{pla} and L_{in}) from DPS events, and the original histograms of the instantaneous bandwidth and the starting frequency are in almost the same range of Bárta et al. (2008). The typical duration of DPSs is 0-60 s (Fig. 11(d)). The reconnection rate derived from the DPS events of cases (I)+(II) and (III) is typically less than 0.04 (Fig. 11(e) and 11(f)). This is comparable to the ones found in previous studies (M_A =0.001-0.1, e.g. Tsuneta et al. 1997; Ohyama & Shibata 1997; Yokoyama et al. 2001; Isobe et al. 2002; Asai et al. 2004; Narukage & Shibata 2006; Takasao et al. 2012).

Then what determines and/or controls the reconnection rate? The dependence of the reconnection rate on the plasmoid velocity, the width (size), the plasma beta, and the aspect ratio of a current sheet attached below a plasmoid is shown in Figures 12(a)-12(e) for cases (I)+(II) and (III). The reconnection rate has a good correlation with the plasmoid velocity. This tendency is retained even after normalizing the plasmoid velocity by the Alfvén velocity. On the other hand, the width and the aspect ratio of plasmoids are weakly correlated with the reconnection rate (Figs. 12(c) and 12(d)). The plasma beta is mainly distributed in the low beta regime (0.02-0.04), and it seems that the distribution of the reconnection rate is broader

with smaller plasma beta. Furthermore, the relationship between the ejection velocity and the width of plasmoids is shown in Figure 12(f). For larger plasmoid with $W_{pla} > 10^9$ cm, the plasmoid velocity tends to become smaller as the size becomes larger. This is probably because the larger plasmoids are heavier and are consequently more decelerated by the gravity force than smaller plasmoids. This result is consistent with Bárta et al. (2008). On the other hand, for smaller plasmoids with W_{pla} <6 $\times 10^8$ cm, the plasmoid velocity tends to increase as the width of the plasmoid increases. This may indicate that larger plasmoid induces stronger inflow, enhancing the reconnection rate and accelerating itself by the faster reconnection outflow.

4.3. Correspondence with EUV and X-ray Plasmoid ejection

Next we compared DPS events with imaging observations in EUV emissions taken by the Atmospheric Imaging Assembly (AIA) on board SDO, to identify a possible correlation between DPSs and plasmoids seen in the EUV corona. Since the temporal resolution of AIA is limited to 12 s, only long-duration DPS events (>1 minutes) observed after SDO launch are used for analysis.

Figure 13(a)-(c) shows snapshot images of a flare event on 2012 June 13 taken with the AIA 94 Å filter. The event shows a plasma ejection in the south-east direction between 12:32-13:17 UT. The loops are gradually moving outward around 12:32 UT and the motion accelerates at 12:53 UT up to an apparent velocity of 2×10^6 cm s^{-1}. In this event, there are no RHESSI data, but the steepest slope of the GOES SXR flux was observed at the beginning of the outward motion. In the 211 Å images small plasma blobs are seen to move in the trailing region of the outward-moving loops. We found a downward motion blob during 12:50:33-12:51:09 UT, and then two small plasma blob ejections between 12:51:57-12:52:33 UT. The radio spectrograph data during the same period is shown in Figure 13(b). There are three periods of DPS: a downward-in-height (upward-in-frequency) DPS (12:50:00 UT), a constant frequency DPS (12:50:40 UT), and an upward-in-height (downward-in-frequency) DPS (12:52:30 UT). The upward motion of the DPS after 12:52:30 UT corresponds to the timing of the outward moving coronal loops observed in 94 Å and the upward velocity of the DPS is 2×10^7 cm s^{-1}, which is much larger than the apparent velocity (2×10^6 cm s^{-1}). The downward motion of the DPS after 12:50 UT has no clear corresponding features in 94 Å images, but small scale blobs in 211 Å images may be candidates to explain the observed DPSs.

Figure 14(a) shows a flare event on 2012 May 8, which shows footpoint brightenings followed by multiple plasma ejections and a loop expansion: the initial ejection at 13:05:26

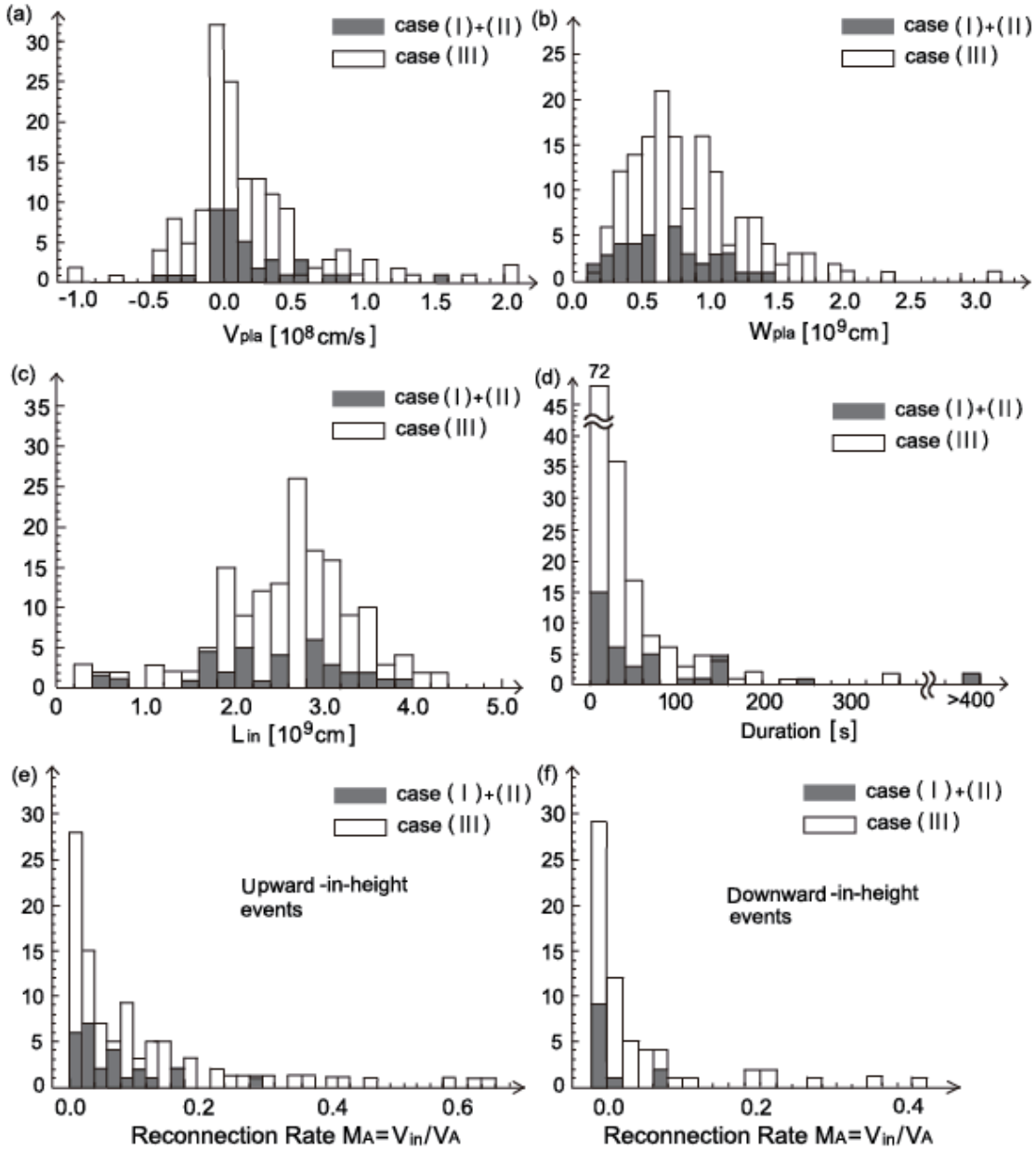

Fig. 11.— Histograms of the distributions of (a) the ejection velocity, (b) the width and (c) the height of plasmoids, (d) the duration and (e)-(f) the reconnection rate during the upward/ downward-in-height plasmoid ejections, which are derived from the DPS events of cases (I)+(II) and (III) during 2002-2012.

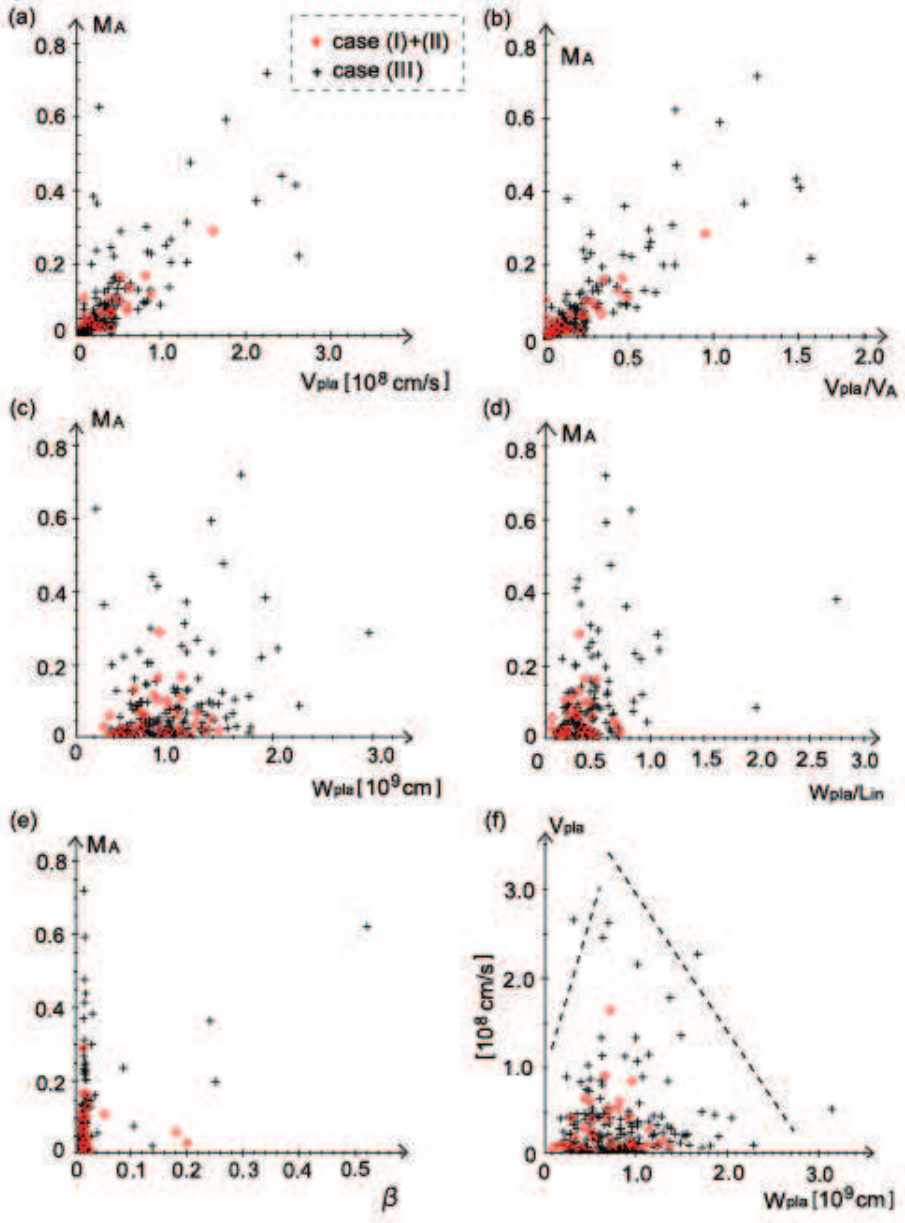

Fig. 12.— (a)-(e) Correlation study for cases (I)+(II) and (III), showing the dependence of the reconnection rate on the original plasmoid velocity, the plasmoid velocity normalized by the local Alfvén velocity, the plasmoid width, the aspect ratio of the reconnection region (i.e. the ratio of the width and the length of a current sheet formed below a plasmoid) and the plasma beta. (f) The relationship between the velocity and the width of plasmoids.

UT, the second one at 13:06:02 UT, the loop expansion during 13:07-13:08 UT and the third ejection at 13:08:02 UT. The radio spectrum of DPSs is shown in Figure 14(i), in which three DPSs are observed: a slow rising-in-height DPS (13:04:50 UT), a downward-in-height DPS (13:07:00 UT) and another slow rising-in-height DPS (13:07:20 UT). The first upward-in-height DPS occurred at the beginning of the first and the second eruptions in 94 Å and 193 Å images, the second downward-in-height DPS is during the loop expansion above the active region but there seems to be no clear corresponding moving feature, and the third DPS is at the beginning of the double plasma ejection.

Figure 15(a) shows an east-limb flare event on 2012 July 6. In 304 Å images, a cool prominence upward motion (marked by an arrow) was observed around 13:28-13:30 UT, which was located below a cavity observed in 94 Å images and at the footpoint of the dark open field lines in the 131 Å images. In the 304 Å snapshot images, small scale intermittent plasma movements are also observed inside the loop structure, apart from the previous prominence. On the other hand, an upward(-in-height) DPS occurred at 13:29:22 UT (Fig. 15(b)), when the cool prominence in 304 Å showed upward motion and when the slope of the GOES SXR flux became the steepest. The apparent upward velocity is $1\times\ 10^6$ cm s^{-1} which is the vertical velocity on the limb, while the upward velocity estimated from the DPS is 1×10^7 cm s^{-1}. The later radio burst after 13:30:25 UT may be related to the inner plasma flow inside the coronal loop structure.

Here we note that, in the paper by Bárta et al. (2008) and also in the present study, we found that the DPS with larger instantaneous bandwidth usually drifts slower than that with smaller bandwidth. It means that larger plasmoids move slower than smaller ones. It is highly probable that in the current sheet there are several plasmoids with different sizes. In EUV we recognize only the largest plasmoid and this EUV plasmoid need not be the same as the plasmoid, where the DPS is generated. It may explain the difference in the velocity of the EUV plasmoid and that derived from the DPS on 2012 July 6. It is true that the size (width) of the observed EUV plasmoids is in the range of 5"-40", i.e. $(0.4\text{-}3.6)\times10^9$ cm. This is comparable to but a little larger than the typical width of the DPS plasmoids $(0.3\text{-}1.1)\times10^9$ cm.

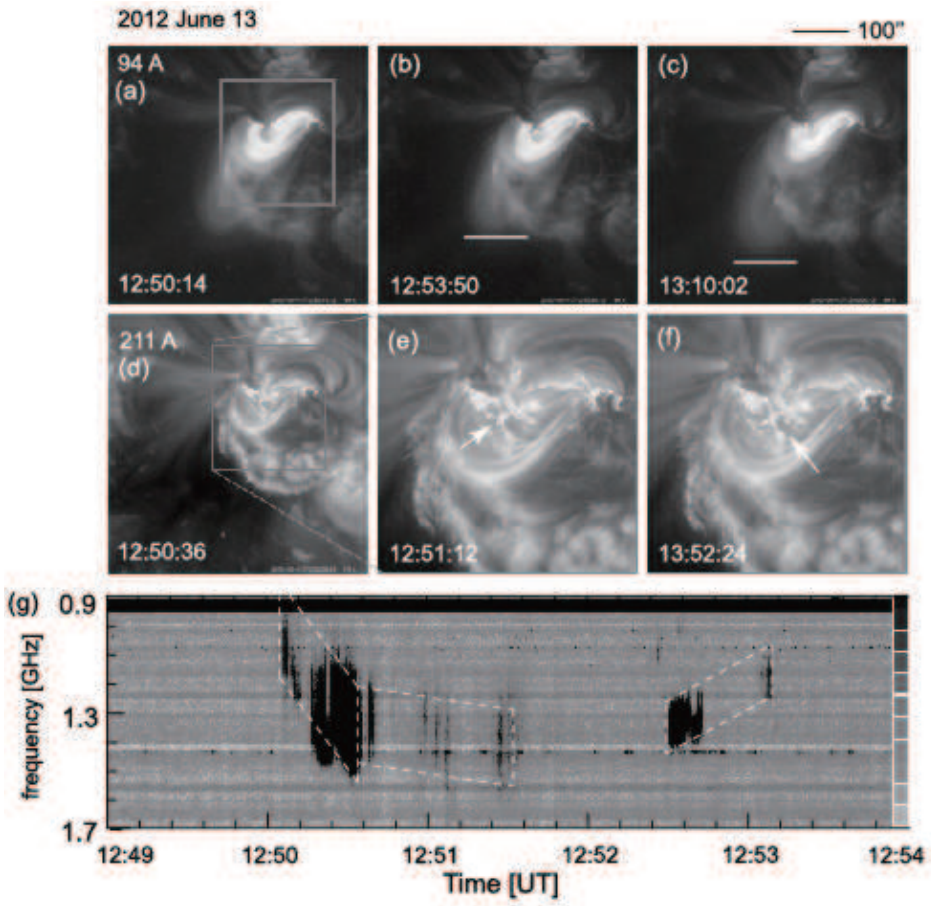

Fig. 13.— (a)-(f) Snapshot images of a flare event on 2012 June 13, taken by 94 and 211 Å filters of AIA/SDO. In (b) and (c), the front of a plasma ejecta is shown by a solid line. (e)(f) are zoom-up images of (d) taken by 211 Å whose field-of-view is shown by a square line in (d). Arrows show small plasma blobs moving in the coronal loops. (g) A radio spectrum of DPSs on 2012 June 13, taken by the radiospectrograph telescope in Ondřejov observatroy.

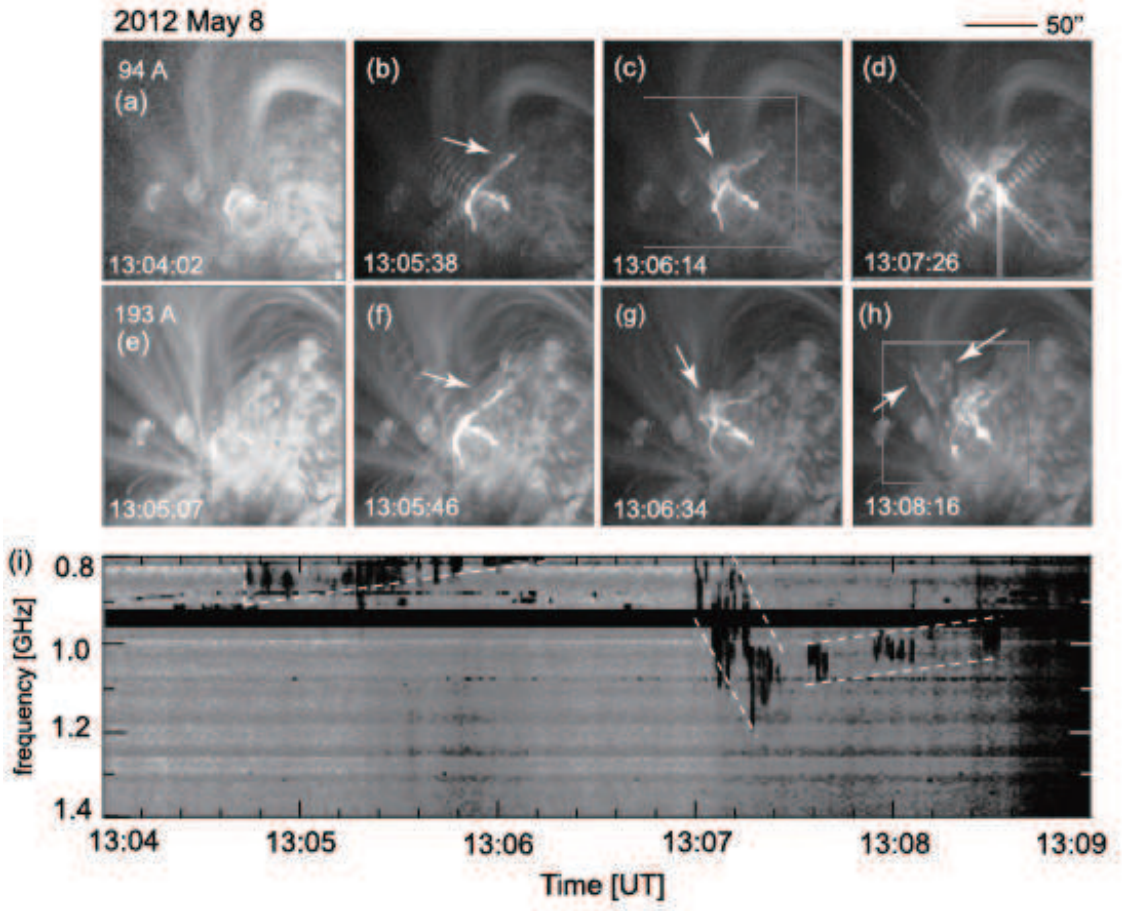

Fig. 14.— (a)-(h) Snapshot images of a flare event on 2012 May 8, taken by 94 and 193 Å filters of AIA/SDO. The event shows two ribbon structure and plasma ejections marked by arrows. (i) A spectrum of DPSs on 2012 May 8, taken by the radiospectrograph telescope in Ondřejov observatory.

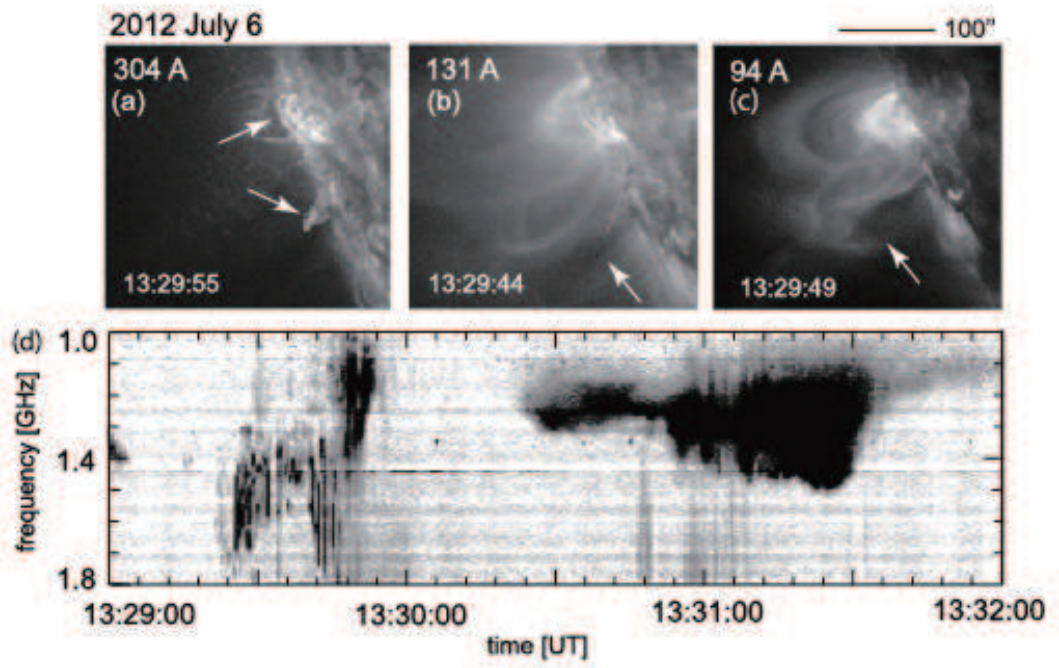

Fig. 15.— (a)-(c) Snapshot images of a flare event on 2012 July 6, taken by 304, 131 and 94 Å filters of AIA/SDO at almost the same time. Arrows in (a) show moving cool plasma in coronal loops (above) and an eruption of a cool plasma (below). In (b)(c), a cavity is shown by an arrow, which is located at the footpoint of the cool plasma ejection observed in 304 Å images.

5. Summary and Discussion

We statistically analyzed 106 DPS events in the frequency range of 0.8-4.5 GHz, observed with radiospectrographs in Ondřejov observatory between 2002 and 2012. The number of DPSs increases with the solar activity, and it peaked at around 2002 and 2012. The DPSs were classified into 4 groups: (I) single events with a constant frequency drift [12 events], (II) multiple events occurring in the same flare with constant frequency drifts [11 events], (III) single or multiple events with increasing or decreasing frequency drift rates [52 events], and (IV) complex events containing multiple events occurring at the same time in the different frequency range [31 events]. Most of the DPS events show an increase or a decrease in their frequency drifts. 70% of DPSs drifted toward lower frequency, while 30% drifted toward larger frequency. In other words, interpreting DPSs as plasmoids, most plasmoid ejections are accelerated or decelerated, and 70% of plasmoids are ejected upward and 30% downward.

Of the DPS events with simultaneous RHESSI observations, 90% of events occurred in association with HXR bursts, mainly in the energy range of 15-25 keV, and they occurred at the beginning or at the peak time of HXR burst. 90% of DPSs were associated with the peak of the GOES SXR gradient and/or RHESSI HXR burst. With the exception of the large flares, HXR photons with energy 25 keV is typically produced by nonthermal electrons, whereas the origin for the HXR in the energy range of 15-25 keV is a mixture of thermal and nonthermal electrons. This is why our result indicates that most of the events are associated with particle acceleration and partially plasma heating. 5 events were observed with radio bursts known as the broadband continuum (type IV burst), and they occurred at the beginning of the radio bursts in the higher frequency range, except for one event. When the duration of the HXR burst was long, multiple DPSs occurred.

Interpreting DPSs as signatures of plasmoids, we measured the ejection velocity, the width and the height of a plasmoid, from which we estimated the inflow velocity and the reconnection rate by considering the mass conservation of incompressible plasma: the velocity 0-5$\times10^7$ cm s^{-1}, the width (0.3-1.1)$\times10^9$ cm, the height (= the current sheet length) (1.8-3.6)$\times10^9$ cm, the duration 0-60 s, and the reconnection rate 0-0.04. The width is smaller than the height of the plasmoid, but they are comparable to each other (consistent with Bárta et al. (2008)). This means that DPS plasmoids are observed in the lower corona, just after the formation and the ejection. This is different from other events of larger X-ray plasmoid ejection (e.g. Glesener et al. 2013). There is a positive correlation between the reconnection rate and the ejection velocity, while the aspect ratio of a current sheet has no clear correlation with the reconnection rate. For larger plasmoid (W_{pla} $>10^9$ cm), the plasmoid velocity tends to decrease as the size becomes larger, whereas for smaller plasmoids (W_{pla} $<6\times10^8$ cm), the plasmoid velocity tends to increase as the width of the plasmoid increases. This is

probably because the larger plasmoids are heavier and are consequently more decelerated by the gravity force than smaller plasmoids. When plasmoids are small, the gravity force is too small to affect the plasmoid dynamics, rather the plasmoid velocity increases as the width of the plasmoid increases, probably because larger plasmoids induces more inflow, enhancing the reconnection rate and additionally accelerates themselves by fasten reconnection outflow.

Some of the DPSs show plasmoid counterparts in AIA images, i.e. plasma ejections or blobs, but others are not clear. This is probably because the emission mechanisms of DPSs and EUVs are different and because the time scale of DPSs is too short compared with the AIA time cadence. DPSs are always associated with HXR in 15-25 keV, but not always in 25-100 keV. Power-law indices of HXR spectra are soft. This indicates that the DPS emission mechanism is not determined by the energy of particles but rather by the condition of the bump-in-tail distribution in electron velocity ($dF(v)/dv > 0$ for $v > 0$; $F(v)$ being the velocity distribution function), which produces the instability for which a wave-particle interaction occurs.

In laboratory experiments, the reconnection electric field is enhanced when a plasmoid is ejected out of a current sheet (Ono et al. 2011; Hayashi et al. 2012). This enables a more efficient particle acceleration and a reconnection rate enhancement, which is consistent with our results. It is also noted that a larger plasmoid ejection leads to a larger enhancement of the electric field and thus a larger reconnection rate in laboratory experiments. However, in our analysis as well as that of Bárta et al. (2008), smaller plasmoids induce a larger reconnection rate. This is probably because larger plasmoids in the solar atmosphere are decelerated by the gravity force, which does not play a strong effect in a laboratory confined plasma configuration. This can explain the differences between laboratory experiments and the solar atmosphere.

The intensity of HXR emission can be described by using Neupert effect as follows;

$$I_{HXR} \propto \frac{dI_{SXR}}{dt} \propto \frac{dEth}{dt} \sim \frac{dEkin}{dt} = \frac{d}{dt}\left(\frac{mv_{pl}^2}{2}\right) = mv_{pl} \cdot \frac{dv_{pl}}{dt} \tag{14}$$

Here we assumed equipartition of released energy to thermal and kinetic energies. This indicates a positive correlation between the HXR intensity and the plasmoid velocity and acceleration. Since the HXR intensity is empirically believed to be proportional to the reconnection rate (Asai et al. 2004), the plasmoid velocity is also proportional to the reconnection rate, as well as equation (1) proposed in plasmoid-induced reconnection model (Shibata & Tanuma 2001).

We classified 106 DPSs into 4 cases and mainly analyzed cases (I)-(III). Case (IV) shows multiple DPSs at the same time individually moving upward and downward. Some

DPSs in case (IV) show merging and separation processes, which may indicate that the coalescence and split of plasmoids take place. With recent numerical simulations, multiple plasmoid forming at different scales in a current sheet and particle accelerations in association with plasmoid dynamics have been intensively studied. The comparison between the events occurring in the corona and simulations may give us further understandings of energy release by magnetic reconnection and particle acceleration, and the onset of flares, eruptions and radio bursts.

We first acknowledge an anonymous referee for his/her useful comments and suggestions. This work was supported in part by JSPS KAKENHI Grant Number 24740132 and in part by the JSPS Core-to-Core Program 22001. MK and MB acknowledge the support by grant P209/12/0103 (GA CR).

REFERENCES

Alvarez, H. & Haddock, F. T., 1973, Sol. Phys., 30, 175

Asai, A., Yokoyama, T., Shimojo, M., Masuda, S., Kurokawa, H. & Shibata, K., 2004, ApJ, 611, 557

Aschwanden, M. J. & Benz, A. O., 1997, ApJ, 480, 825

Aschwanden, M. J., Newmark, J. S., Delaboudiniére, J.-P., et al., 1999, ApJ, 515, 842

Aschwanden, M. J., 2002, Space Sci. Rev., 101, 1

Aschwanden, M. J., 2004, Physics of the solar corona, Springer, Praxis Publ. Chichester, UK

Bain, H. M. , Krucker, S., Glesener, L. & Lin, R. P., ApJ, 2012, 750, 44

Bárta, M., Karlický, M & Žemlička, R., 2008, Sol. Phys., 253, 173

Bárta, M., Skála, J., Karlický, M., & Büchner, J., 2012, Multi-scale Dynamical Processes in Space and Astrophysical Plasmas, Astrophysics and Space Science Proc., 33, 43 (Springer-Verlag Berlin Heidelberg 2012)

Bárta, M., Büchner, J., Karlický, M., & Skála, J., 2011, ApJ, 737, 24

Benz, A. O., Grigis, P. C., Csillaghy, A., Saint-Hilaire, P., 2005, Sol. Phys., 226, 121

Drake, J. F., Swisdak, M., Che, H. & Shay, M. A., 2006, Nature, 443, 553

Dulk, G. A. & McLean, D. J., 1978, Sol. Phys., 57, 279

Dulk, G. A., Goldman, M. V., Steinberg, J. L., & Hoang, S., 1987, A&A, 173, 366

Fárník, F., Garcia, H., & Karlický, M., 2001, Sol. Phys., 201, 357

Glesener, L., Krucker, S., Bain, H. M., Lin, R. P., 2013, ApJ, 779, 29

Hayashi, Y., Ii, T., Inomoto, M., & Ono, Y., 2012, IEEJ Transactions on Fundamentals and Materials, 132, 239

Hoshino, M., 2012, PRL, 108, 135003

Hudson, H. S., Kosugi, T., Nitta, N. V., & Shimojo, M., 2001, ApJ, 561, L211

Isobe, H., Yokoyama, T., Shimojo, M., et al., 2002, ApJ, 566, 528

Jiřička, K., Karlický, M., Kepka, O., & Tlamicha, A., 1993, Sol. Phys., 147, 203

Karlický, M., Fárník, F. & Mészárosová, H., 2002, A&A, 395, 677

Karlický, M. 2004, A&A, 417, 325

Karlický, M., Fárník, F., & Krucker, S., 2004, A&A, 419, 365

Karlický, M., & Bárta, M., 2011, ApJ, 733, 107

Khan, J. I., Vilmer, N., Saint-Hilaire, P., & Benz, A. O., 2002, A&A, 388, 363

Kliem, B. Karlický, M., & Benz, A. O., 2000, A&A, 360, 715

Kolomański, S. & Karlický, M., 2007, A&A, 475, 685

Krucker, S., Hudson, H. S., Glesener, L., et al. 2010, ApJ, 714, 1108

Kumar, P. & Cho, K.-S., 2013, A&A, 557, A115

Kundu, M. R., Nindos, A., Vilmer, N., et al., 2001, ApJ, 559, 443

Lin, J. & Forbes, T. G., 2000, JGR, 105, 2375

Lin, R. P., Dennis, B. R., Hurford, G. J., et al., 2002, Sol. Phys., 210, 3

Liu, R., Lee, J., Wang, T., et al., 2010, ApJ, 723, L28

Liu, W., Chen, Q., & Petrosian, V., 2013, ApJ, 767, 168

Milligan, R. O., McAteer, R. T. J., Dennis, B. R., & Young, C. A., 2010, ApJ, 713, 1292

Narukage, N. & Shibata, K., 2006, ApJ, 637, 1122

Neupert, W. M., 1968, ApJ, 153, L59

Nishida, K., Nishizuka, N., & Shibata, K., 2013, ApJ, 775, L39

Nishizuka, N., Takasaki, H., Asai, A., & Shibata, K., 2010, ApJ, 711, 1062

Nishizuka, N. & Shibata, K., 2013, PRL, 110, 051101

Ohyama, M., & Shibata, K., 1997, PASJ, 49, 249

Oka, M., Phan, T.-D., Krucker, S., et al., 2010, ApJ, 714, 915

Ono, Y., Hayashi, Y., Ii, T., et al., 2011, Phys. Plasmas 18, 111213

Priest, E. R., 1985, Reports on Progress in Physics (ISSN 0034-4885), 48, 955

Reeves, K. K., & Golub, L., 2011, ApJ, 727, L52

Reid, H. A. S., Vilmer, N., & Kontar, E. P., 2011, A&A, 529, A66

Savage, S. L., McKenzie, D. E., Reeves, K. K., Forbes, T. G., & Longcope, D. W., 2010, ApJ, 722, 329

Shibata, K., Masuda, S., Shimojo, M., et al., 1995, ApJ, 451, L83

Shibata, K., & Tanuma, S., 2001, Earth Planets Space, 53, 473

Shimizu, T., Kondoh, K., Shibata, K., & Ugai, M., 2009, Phys. Plasmas, 16, 052903

Sui, L., & Holman, G. D., 2003, ApJ, 596, L251

Takasao, S., Asai, A., Isobe, H., & Shibata, K., 2012, ApJ, 745, L6

Tan, B., Yan, Y., Tan, C., & Liu, Y., 2007, ApJ, 671, 964

Tan, B., 2008, Sol. Phys., 253, 117

Tan, C., Yan, Y. H., Liu, Y. Y., et al., 2008, Advances in Space Research, 41, 969

Tanaka, K. G., Yumura, T., Fujimoto, M., et al., 2010, Phys. Plasmas, 17, 102902

Temmer, M., Veronig, A. M., Vršnak, B., et al., 2008, ApJ, 673, L95

Tsuneta, S., Masuda, S., Kosugi, T., & Sato, J., 1997, ApJ, 478, 787

Wang, R., Tan, B., Tan, C., & Yan, Y., 2012, Sol. Phys., 278, 411

Webb, D. F., Burkepile, J., Forbes, T. G. & Riley, P., 2003, JGR, 108, 1440

Wild, J. P., Roberts, J. A. & Murray, J. D., 1954, Nature, 173, 532

Yokoyama, T., Akita, K., Morimoto, T., et al., 2001, ApJ, 546, L69

Zhang, J., Dere, K. P., Howard, R. A., et al., 2001, ApJ, 559, 452

This preprint was prepared with the AAS LaTeX macros v5.2.